Research Square

Preprints are preliminary reports that have not undergone peer review.
They should not be considered conclusive, used to inform clinical practice,
or referenced by the media as validated information.

Three-dimensional computational modeling of magnetic hyperthermia: the role of blood perfusion in selectivity and dosimetric optimization

Matheus Fernandes Muniz de Almeida

matheus.fern1337@gmail.com

Southwest Bahia State University

Emily Lauri Santos Araujo

Simara Santos Campos

Southwest Bahia State University

Luizdarcy de Matos Castro

Southwest Bahia State University

Research Article

Keywords: Magnetic hyperthermia, Computational model, Bioheat transfer, Thermal dosime- try, Cancer therapy

Posted Date: September 21st, 2026

DOI: https://doi.org/10.21203/rs.3.rs-11065417/v1

License: This work is licensed under a Creative Commons Attribution 4.0 International License.
Read Full License

Additional Declarations: No competing interests reported.

Three-dimensional computational modeling of magnetic hyperthermia: the role of blood perfusion in selectivity and dosimetric optimization

Matheus Fernandes Muniz de Almeida[1], Emily Lauri Santos Araujo[2], Simara Santos Campos[3], Luizdarcy de Matos Castro[4]

[1] matheus.fern1337@gmail.com, Southwest Bahia State University, Vitoria da Conquista, Bahia, Brazil - ORCID 0009-0009-3576-5381;

[2]emily.laraujo6@gmail.com, Southwest Bahia State University, Jequie, Bahia, Brazil;

[3] simaracampos@uesb.edu.br Southwest Bahia State University, Department of Exact and Technological Sciences, Vitória da Conquista, Bahia, Brazil - ORCID 0000-0002-0616-2030;

[4]luizdarcy.castro@uesb.edu.br Southwest Bahia State University, Department of Exact and Technological Sciences, Vitoria da Conquista, Bahia, Brazil - ORCID 0000-0002-1922-5168

Abstract

Purpose: This work's aim was to develop a three-dimensional computational model for predictive simulation and dosimetric optimization of magnetic hyperthermia (MH), and to investigate blood perfusion's role in enhancing its selectivity.

Methods: The Pennes bioheat equation was solved numerically in Julia using finite differences on a 2.0 cm cubic domain containing concentric spherical tumor (radius 4.0 mm; volume ≈268 mm^3). The model coupled Arrhenius thermal damage, nonlinear perfusion, and CEM43. Heat generation used SAR via Rosensweig's linear response theory, including log-normal nanoparticle size polydispersity (mean diameter 20 nm; σ=0.18) and Gauss–Hermite quadrature. Parameters were calibrated against in vivo sarcoma 180 data under an alternating magnetic field of 301 kHz and 220 G.

Results: Tumor temperature stabilized at 47.97°C after ∼15 min; healthy tissue remained at 38.18°C. Tumor perfusion initially peaked at 1.28×10^{-3} s^{-1} at 98 s, then decreased about 90.31%; healthy tissue perfusion increased about 49.89% before a late decrease of 14.35%. At 1800 s, 100% of tumor points exceeded the irreversible damage threshold ($\theta \geq 0.75$), with mean damage 0.988 and complete ablation by 1780s. Healthy tissue showed no irreversible damage (mean $\theta = 0.336$). For CEM43, 83.33% of tumor volume received more than 240 min (mean 1503.75 min), whereas healthy tissue averaged 1.69 min.

Conclusion: The model reproduced key in vivo thermal and vascular dynamics, supporting its use for rapid, reproducible, and cost-effective optimization of MH protocols while reducing reliance on preclinical animal testing.

Keywords: Magnetic hyperthermia, Computational model, Bioheat transfer, Thermal dosimetry, Cancer therapy.

Introduction

Cancer remains one of the greatest challenges facing global public health, and its incidence has been rising in recent decades. Studies indicate that, over the past 10 years, there has been a 20% increase in incidence, and it is expected that by 2030, there will be more than 25 million new cases (Santos *et al.*, 2023). Although conventional approaches remain the cornerstones of cancer treatment, they often have limited efficacy in certain situations and may be accompanied by resistance and toxicity, leading to adverse effects (Rodrigues, 2017).[1]

Consequently, there is a growing demand for complementary therapeutic alternatives that are minimally invasive and highly selective, enabling targeted treatment of the tumor without inflicting severe damage on the body.

In this context, magnetic hyperthermia (MH) stands out for its high selectivity and promising results in fighting cancer, as it minimizes risks and side effects while also enhancing the efficacy of traditional treatments, such as chemotherapy and radiation therapy. The treatment consists of controlled heating of a specific tumor region to induce cell destruction, exploiting the lower heat tolerance of neoplastic cells (Maniotis; Maragakis; Vordos, 2025). To achieve this, superparamagnetic nanoparticles are injected into the tumor microenvironment; under the influence of an alternating magnetic field, these nanoparticles heat up and promote localized destruction.

In addition, MH exhibits remarkable synergy when used as an adjunct to traditional therapies: when combined with chemotherapy, it increases microvascular permeability and intratumoral drug uptake, while when used in conjunction with radiation therapy, it acts as a potent radiosensitizer by inhibiting DNA repair mechanisms and reducing radiation resistance due to hypoxia (Almeida; Campos; Castro, 2026; Rodrigues, 2017).

However, as detailed by Almeida, Campos, and Castro (2026), one of the main barriers to the clinical advancement of MH is the lack of methodological standardization regarding field frequency and intensity, thermal dose, and nanoparticle dose. This compromises the reproducibility of protocols and hinders control of the thermal dose.

In this context, the objective of this study is to develop a three-dimensional computational model for predictive simulation and dosimetric optimization. Developed in the Julia programming language, the simulator numerically solves the Pennes equation (Pennes, 1948) in a controlled geometry, allowing for the reproduction of real thermal dynamics and the systematic evaluation of dozens of distinct therapeutic scenarios and protocols by varying their parameters. This enables the rapid, cost-effective, and reproducible exploration of dosimetric guidelines, helping to reduce reliance on preclinical trials.

Specifically, this study focuses on exploring the role of blood perfusion, demonstrating that the dysplastic vasculature present in the tumor—which plays a central role in the development of resistance to other therapies—is the primary factor enhancing the selectivity of MH.

[1] Doctoral thesis - Hipertermia magnética in vivo com nanopartículas de MnFe2O4 no tratamento de tumores sólidos e subcutâneos de Sarcoma 180. Harley Fernandes Rodrigues, 2017.

Magnetic hyperthermia

Magnetic hyperthermia is emerging as an innovative, highly selective therapeutic approach based on the controlled and localized heating of the tumor region to induce the death of neoplastic cells, taking advantage of their lower thermal tolerance compared to healthy tissue. To achieve this, superparamagnetic nanoparticles are injected into the tumor microenvironment, and an external magnetic field is applied to heat the particles.

Preclinical evidence accumulated over the past decades demonstrates the antineoplastic potential of magnetic hyperthermia (MH). In in vitro assays, exposing human tumor cell lines to temperatures ranging from 42°C to 45°C for intervals of 30 to 60 minutes reduced cell viability by significant rates ranging from 60% to 90% (Vilas-Boas; Carvalho; Espina, 2020).

In *in vivo* animal models, preclinical studies have demonstrated the technique's efficacy in the regression and elimination of solid tumors. Trials conducted in Wistar rats with C6 glioma brain tumors treated with aminosilane-coated magnetite nanoparticles revealed a 32.8% reduction in tumor mass (Rego *et al.*, 2019). Similarly, studies conducted in mice have demonstrated the potential of MH to inhibit metastasis in cases of gastric cancer that has spread to the peritoneal cavity (Matsumura *et al.*, 2021).

In human research, MH has shown promising results in clinical trials for glioblastoma multiforme and prostate cancer. In the treatment of recurrent prostate cancer, Phase I clinical trials with iron oxide nanoparticles induced a significant decline of 25% to 70% in PSA levels in 80% of the patients evaluated (Johannsen *et al.*, 2007). In patients with recurrent glioblastoma multiforme, a Phase II study combined MH with radiation therapy, achieving a median overall survival of 23.2 months from the primary diagnosis, representing a significant survival benefit compared to conventional treatments (Maier-Hauff *et al.*, 2011). Recently, a clinical evaluation of the "NanoPaste" technique applied to the margins of the post-surgical resection cavity in glioblastomas demonstrated its ability to induce necrosis and promote a potent antitumor immune response, characterized by local infiltration of CD3+ and CD8+ T lymphocytes (Grauer *et al.*, 2019).

The therapeutic efficacy of MH is significantly enhanced when used as an adjunct to conventional cancer therapies. As an adjunct to radiation therapy, thermal stress acts as a potent sensitizer that inhibits the DNA repair pathways of radiation-damaged neoplastic cells (Peeken; Vaupel; Combs, 2017). In addition, moderate local heating promotes vasodilation and increased blood flow to the tumor, which improves oxygenation, partially reverses the radioresistance associated with hypoxia, and enhances the uptake of chemotherapeutic agents (Rodrigues, 2017).

Despite notable advances, the incorporation of MH into clinical practice still faces serious challenges. The first obstacle lies in the limited systemic delivery of the nanoparticles, since only a fraction of the dose administered intravenously reaches the tumor microenvironment, necessitating the use of direct injections (Rodrigues; Capistrano; Bakuzis, 2020). Additionally, the heterogeneous spatial distribution of the material within the tumor can create cold spots that limit the effectiveness of ablation.

Furthermore, the lack of methodological standardization, the scarcity of controlled

clinical data, difficulties in standardizing the production of nanoparticles and their biocompatible coatings, and the absence of robust clinical protocols for validating the technique are problems that need to be overcome (Almeida; Campos; Castro, 2026). Furthermore, although animal models continue to play an important role in evaluating the efficacy and safety of new cancer interventions, genetic, molecular, and physiological limitations often restrict their usefulness. Despite success in preclinical trials, 85% of initial clinical trials of new drugs fail; of those that advance to Phase III, only half are approved for use. The highest proportion of these failures occurs in trials of anticancer drugs (Mak; Evaniew; Ghert, 2014). This critical scenario stems from species-specific incompatibilities. In the context of MH, this disconnect manifests directly in dosimetric safety; computational studies reveal that thermal parameters originally established based on small mice (such as the Hergt-Dutz threshold) fail severely when extrapolated to larger specimens, in which eddy currents are induced, potentially causing unintended burns (Vicentini et al., 2022).

Given these limitations of scale and species, predictive models based on three-dimensional numerical simulations emerge as important tools by enabling the rapid, inexpensive, and reproducible testing of dozens of scenarios, thereby reducing reliance on preclinical animal testing.

Methods

Bioheating Equation

The bioheating equation (Pennes, 1948) is one of the most widely used mathematical models for describing heat transfer in biological tissues. Physiologically, the thermal energy balance in tissue takes into account the contribution of various biophysical phenomena, which is mathematically expressed as a parabolic partial differential equation:

$$\rho c_p \frac{\partial T}{\partial t} = k\nabla^2 T + \rho_b c_b \omega_b (T_b - T) + Q_m + Q_{SAR} \tag{1}$$

where ρ and c_p represent, respectively, the density and specific heat of the biological tissue, T is the transient local temperature; t denotes time; and k is the thermal conductivity of the medium. On the right-hand side of the equation, the first term models heat diffusion by conduction through the tissue. The second term accounts for the heat exchange induced by blood perfusion, where ρ_b is the density of blood, c_b is the specific heat of arterial blood, T_b is the body's basal arterial temperature, and ω_b represents the local blood perfusion rate. The third term, Q_m quantifies basal metabolic energy generation; finally, the SAR source term describes the thermal power dissipated by the nanoparticles under the action of the magnetic field.

Modeling of perfusion and damage.

In addition, there are models that treat the microvascular perfusion rate as nonlinear and dependent on thermal stress and accumulated cellular damage. The vascular system responds to heating in a biphasic manner: initially, at moderate temperatures, compensatory vasodilation occurs, increasing blood flow to enhance heat dissipation; however, prolonged exposure to high temperatures induces severe structural damage that triggers vascular col-

lapse. To reproduce this transient behavior, the local blood perfusion rate b at each node of the three-dimensional mesh, the Arrhenius cumulative thermal damage (Ω) was coupled according to the mathematical formulation presented by Singh, Bhowmik, and Repaka (2020).

$$\omega_b(t) = \begin{cases} \omega_b(t) = \omega_o, & \text{if } \Omega = 0 \\ \omega_b(t) = \omega_o(1 + 25\Omega - 260\Omega^2), & \text{if } 0 < \Omega \leq 0.1 \\ \omega_b(t) = \omega_o e^{-\Omega}, & \text{if } \Omega \geq 0.1 \end{cases} \tag{2}$$

In this formalism, the term o represents the basal blood perfusion rate of each tissue. The function describes three distinct regimes: for $\Omega = 0$ we have normal perfusion and intact tissue; for $0 < \Omega \leq 0.1$, there is an increase in perfusion due to the vasodilation effect and the body's attempt to cool the heated region; finally, for $\Omega \geq 0.1$, there is an exponential reduction in perfusion, followed by vascular collapse and progressive damage.

In addition, there is the Arrhenius thermal damage model, which describes the rate of cellular degradation as a temperature-dependent process. In this formalism, the variable Ω represents the damage accumulated over time, obtained by integrating an exponential rate that depends on the local temperature. Thus, the evolution of thermal damage depends on the model's kinetic parameters, such as the activation energy and the frequency factor, which model how heat-resistant the simulated tissue is (Singh; Bhowmik; Repaka, 2020). The model describes cellular degradation as a chemical reaction dependent on temperature and exposure time. The dimensionless cumulative damage parameter Ω is calculated at each point throughout the treatment using the equation:

$$\Omega(x, y, z, t) = \int_0^t A e^{-\frac{E_a}{R_g T(x,y,z,\tau)}} \, d\tau \tag{3}$$

where E_a is the activation energy for the irreversible thermal damage reaction; R_g is the universal gas constant; T is the tissue temperature; and A is a reaction rate factor. Tissue viability decays exponentially as a function of accumulated damage, as determined by the ratio of surviving cells $e^{-\Omega}$, allowing the fraction of permanently damaged tissue (θ) to be calculated using the equation:

$$\theta(x, y, z, t) = 1 - e^{-\Omega(x,y,z,t)} \tag{4}$$

In post-processing, the critical threshold of $\theta \geq 0,75$ ($\Omega \approx 1,4$) as a conservative criterion for determining the extent of irreversible tissue damage (Capistrano et al., 2020)

At the same time, to express the cumulative effect of time and temperature on a scale that can be correlated with other clinical scenarios, various authors use the thermal dose in terms of Cumulative Equivalent Minutes at 43°C (CEM43), a model originally proposed by Sapareto and Dewey (1984) and widely used in the literature (Rodrigues, Capistrano, and Bakuzis, 2020). The CEM43 model is based on the empirical observation that the cell mortality rate approximately doubles for every 1°C increase above the 43°C breakpoint temperature, exhibiting reduced thermal sensitivity for temperatures below this threshold

due to the development of heat tolerance mediated by heat shock proteins. In the simulation code, the accumulated thermal dose over the $1,800$ seconds of treatment was calculated as:

$$CEM43(x, y, z) = \sum_{i=1}^{M} R^{43-T_i(x,y,z)} \Delta t \tag{5}$$

where M indicates the number of time steps recorded, T_i represents the average temperature in degrees Celsius at that point during the transient interval, Δt is the sampling interval expressed in minutes, and R is the empirical compensation coefficient, defined as $R = 0.5$ for temperatures above 43°C and $R = 0.25$ for temperatures equal to or below 43°C. In line with the dosimetry standards established in the literature for ablative thermal therapies, the critical threshold of CEM43 ≥ 240 minutes was adopted as the indicator of tissue death, serving as a key metric to confirm tumor elimination (Rodrigues, 2017).

Building the Simulation

For the simulation, the computational domain was defined as a cube with dimensions of 2.0 cm. Within this domain, a concentric spherical tumor region with a radius of 4.0 mm was inserted, corresponding to an approximate tumor volume of 268 mm^3. The choice of a tumor model with this radius is justified by its ability to strike a methodological balance between the representativeness of solid tumors and the feasibility of numerical solutions. This sizing is supported by well-established experimental studies, mimicking the volumes of solid tumors commonly evaluated in vivo. Among the references in the literature, the volume considered represents reported ranges for sarcoma 180 (varying between 250 mm^3 and 400 mm^3), human glioblastoma multiforme U87-MG (commonly studied in volumes ranging from 100 mm^3 to 150 mm^3), and C3H murine mammary adenocarcinoma (with volumes ranging from 120 mm^3 to 400 mm^3) (Rodrigues, 2017; Vilas-Boas; Carvalho; Espina, 2020; Rodrigues; Capistrano; Bakuzis, 2020).

Additionally, the use of a cubic-spherical geometric approximation—although it disregards the asymmetry and anatomical irregularities of real tumor masses—is a well-established strategy. This methodological choice is based on reducing the computational load of numerical solvers and on the high technical complexity associated with mapping and generating realistic three-dimensional meshes from data derived from imaging exams (Rodrigues; Capistrano; Bakuzis, 2020). In this regard, Kainz et al. (2019) explain that converting medical image data into realistic geometries requires segmentation and property assignment, and that any subsequent adjustment to the mesh or shape of the actual organ becomes "computationally inefficient," requiring years of effort to create high-fidelity anatomical models. The authors also explain that the first computational phantoms were composed of simple geometric volumes (such as cylinders and spheres) and that modeling using Constructive Solid Geometry allows for the creation of volumetric representations using simple mathematical primitives (spheres, cuboids, ellipsoids) which, although they have "limited anatomical accuracy," are widely accepted and well-established in simulations.

In addition, Rodrigues, Capistrano, and Bakuzis (2020) define the need to reconstruct realistic three-dimensional geometries—in which the Pennes equation must be solved—by

segmenting the region and associating thermal properties with each segment as a "mathematical challenge." They also point out that reconstructions based on actual CT scans often suffer from "low resolution," as they are reconstructed from "few slices."

In this context, the volume of 268 mm^3 is significantly above the minimum physical threshold required for the collective heating effects of the nanoparticles to become biologically dominant relative to peripheral dissipation (Vilas-Boas; Carvalho; Espina, 2020). Thus, the simplified geometric model serves as a standardized control tool, enabling the systematic simulation of different physical and physiological boundary conditions with precision and reproducibility, without introducing numerical instabilities into the simulation.

For the numerical solution of the Pennes PDE, the Finite Difference Method was used to discretize only the spatial operators and convert the system into a coupled set of time-dependent ordinary differential equations. The cubic domain was spatially discretized into a uniform three-dimensional grid with $N_x \times N_y \times N_z$ points, with spacings corresponding to

$$dx = L_x/(N_x - 1), \quad dy = L_y/(N_y - 1) \quad \text{and} \quad dz = L_z/(N_z - 1). \tag{6}$$

The three-dimensional Laplacian operator, $\nabla^2 T = \frac{\partial^2 T}{\partial x^2} + \frac{\partial^2 T}{\partial y^2} + \frac{\partial^2 T}{\partial z^2}$ was approximated by a second-order central difference scheme. To ensure computational efficiency in the assembly of the rigid ODE solver, the global discrete Laplacian L was structured as a large sparse matrix through the use of Kronecker products ($\otimes$):

$$L = (I_z \otimes I_y \otimes D_x) + (I_z \otimes D_y \otimes I_x) + (D_z \otimes I_y \otimes I_x) \tag{7}$$

where I_x, I_y and I_z are identity matrices whose dimensions match the number of nodes on each coordinate axis, while D_x, D_y and D_z are the second-derivative operators of finite differences. The physical coupling with the external environment was established by imposing thermal boundary conditions. Thus, for all points located on the geometric boundaries of the cube, the temperature was set to the basal arterial temperature, $T_{borda} = T_b = 310.15K$. This mathematical formulation replicates the transition with healthy peripheral tissues that are not affected by heat.

The rate of heat generation in the tumor, resulting from magnetic excitation, is modeled using the Specific Absorption Rate (SAR) based on Rosensweig's Linear Response Theory (2002). However, since experimentally synthesized nanoparticles are not entirely homogeneous, modeling a purely monodisperse population tends to overestimate the actual heat generation capacity (Maniotis; Maragakis; Vordos, 2025). Since the anisotropy energy barrier and the relaxation time depend on the nanoparticle's volume, small variations in size can induce changes in its thermal stability and efficiency of coupling with the field. To mitigate this inconsistency, diameter polydispersity was incorporated using a log-normal statistical distribution for the core diameter of the magnetite particles, adopting a nominal average diameter of 20 nm and a standard deviation of 0.18 to mimic the experimental samples. The integration of the power dissipated by the nanoparticles is performed numerically using the Gauss-Hermite quadrature method, which statistically weights the thermal contributions of different fractions of the particle population.

The numerical solution stage of the model begins after the bioheating equation has been discretized. At this point, each point in the spatial grid represents a time-dependent differential equation, and the temperature field is reorganized into a state vector. The time evolution of this vector constitutes the problem to be solved numerically.

At each time step, the solver performs a sequence of operations. Initially, the temperature vector is reorganized into a matrix form corresponding to the spatial grid, allowing for the calculation of the local terms of the equation. Next, the diffusive term is evaluated using central finite differences, taking into account interactions with the immediate neighbors of each point. In parallel, the terms for blood perfusion, metabolism, and the heat source associated with SAR are computed. These terms are combined to form the time derivative of the temperature at each point, which is then returned to the solver.

Simultaneously with the temperature evolution, the thermal damage equation is also solved in a coupled manner. At each evaluation of the system function, the damage rate is calculated for each mesh point based on the instantaneous temperature and is then integrated over time in a manner consistent with the solver's numerical scheme. This implies that thermal damage evolves continuously throughout the simulation, tracking the thermal variations imposed by the heating.

At each time step, after the damage is updated, perfusion is recalculated point by point across the domain. Thus, perfusion becomes a dynamic variable that continuously responds to the thermal state and the level of tissue damage. This coupling between temperature, thermal damage, and perfusion is one of the central aspects of the numerical solution to the problem. Temperature influences thermal damage via the Arrhenius equation; thermal damage, in turn, modifies blood perfusion; and perfusion alters the heat exchange term with blood in the Pennes equation, feeding back into the temperature evolution.

Results and Discussion.

The results obtained are based on a calibration of physical, magnetic, and physiological parameters derived from real biological data. The domain parameterization and the properties of the nanoheaters were calibrated based on the pre- by Rodrigues (2017), in which Swiss mice bearing subcutaneous solid Sarcoma 180 tumors were subjected to MH using manganese ferrite nanoparticles coated with dimercaptosuccinic acid under the action of an alternating magnetic field with a frequency of 301 kHz and an amplitude of 220 Gauss. Additionally, the kinetic constants and the nonlinear vascular perfusion model were parameterized according to Capistrano et al. (2020). To validate whether the thermal evolution dynamics, vascular behavior, accumulated thermal dose (CEM43), and tissue damage fraction (θ) generated by the model are accurate, the results were directly compared with those of Rodrigues (2017) and Capistrano et al. (2020).

The obtained temporal temperature profiles reveal a highly selective bimodal thermal behavior between the tumor and healthy regions. As illustrated in the tumor temperature evolution curves in Figure 1, the average temperature in the tumor rises rapidly in the initial minutes, gradually converging until it reaches and stabilizes at a plateau of 47.97 °C after approximately 15 minutes.

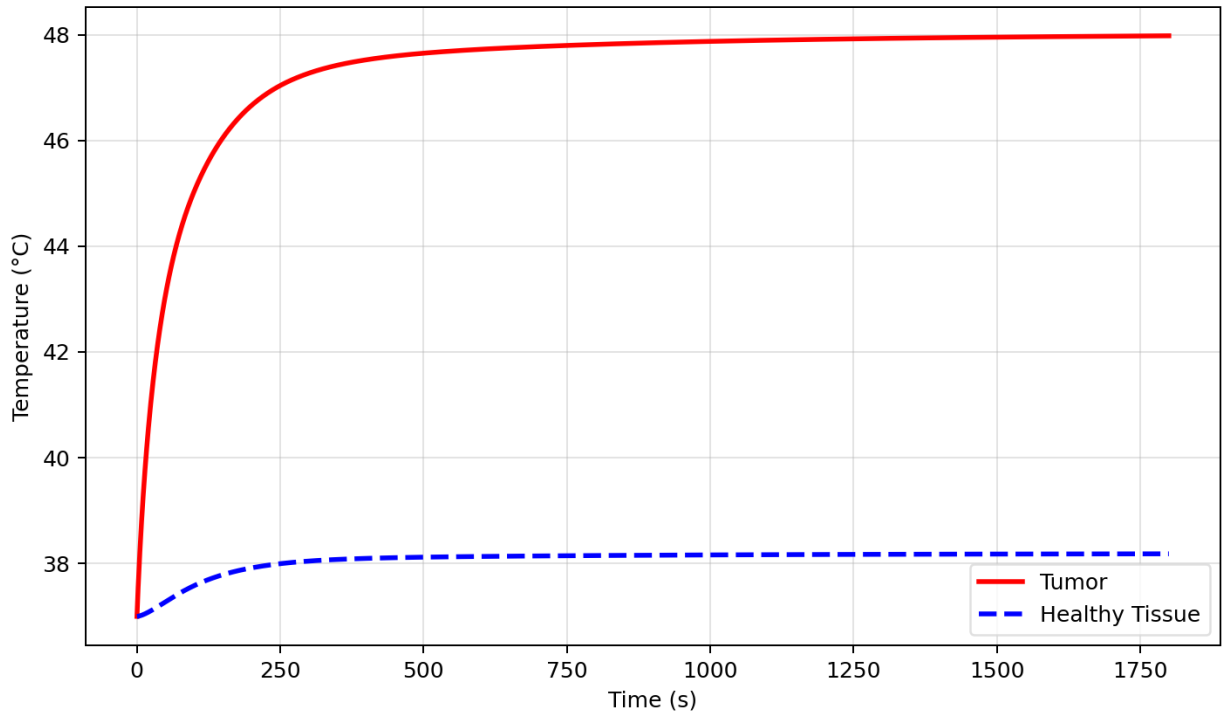


Figure 1: Graphic showing temperature trends over time in different regions.

This localized heating shows a phenomenological correlation with the in vivo experimental data from Rodrigues (2017), who recorded stable intratumoral temperatures in the range of 42°C to 56°C (with stable intratumoral averages of 50.52°C for Animal 1 and 48.39°C for Animal 2). Furthermore, the stabilized temperature of 47.97°C falls within the heating window of 45°C to 50°C reported for the preclinical thermal treatments by Capistrano et al. (2020).

In contrast, the average temperature of the surrounding healthy tissue, shown in Figure 1 in the model, exhibits an extremely modest increase, stabilizing at 38.18°C at the end of the 1,800-second simulation. This behavior of healthy tissue, maintained comfortably below the critical threshold for thermal damage of 43°C, is consistent with the safety readings reported by Rodrigues (2017) in regions distant from the tumor, such as the animal's rectum and abdomen, which ranged up to 37.5°C. This marginal attenuation is due to the active cooling role played by healthy blood perfusion, which benefits from the slight increase in temperature. The formation of a steep and well-defined thermal gradient between the tumor and the healthy margins demonstrates the high spatial selectivity of energy deposition by the nanoparticles.

Furthermore, analysis of the microvascular response to thermal stress reveals highly contrasting and selective nonlinear behavior between regions. As illustrated in the time-course graphs of the tumor and healthy tissue in Figure 2, blood perfusion responds asymmetrically to heating.

This localized heating exhibits a phenomenological correlation with the in vivo ex-

perimental data from Rodrigues (2017), who recorded stable intratumoral temperatures in the range of 42°C to 56°C (with stable intratumoral averages of 50.52°C for Animal 1 and 48.39°C for Animal 2). Furthermore, the stabilized level of 47.97°C falls within the heating window of 45°C to 50°C reported for the preclinical thermal treatments by Capistrano et al. (2020).

In contrast, the average temperature of the surrounding healthy tissue, shown in Figure 1 in the model, exhibits an extremely modest increase, stabilizing at 38.18°C at the end of the 1,800-second simulation. This behavior of healthy tissue, maintained comfortably below the critical threshold for thermal damage of 43°C, is consistent with the safety readings reported by Rodrigues (2017) in regions distant from the tumor, such as the animal's rectum and abdomen, which ranged up to 37.5°C. This marginal attenuation is due to the active cooling role played by healthy blood perfusion, which benefits from the slight increase in temperature. The formation of a steep and well-defined thermal gradient between the tumor and the healthy margins demonstrates the high spatial selectivity of energy deposition by the nanoparticles.

Furthermore, analysis of the microvascular response to thermal stress reveals highly contrasting and selective nonlinear behavior between regions. As illustrated in the time-course graphs of the tumor and healthy tissue in Figure 2, blood perfusion responds asymmetrically to heating.

This localized heating exhibits a phenomenological correlation with the in vivo experimental data from Rodrigues (2017), who recorded stable intratumoral temperatures in the range of 42°C to 56°C (with stable intratumoral averages of 50.52°C for Animal 1 and 48.39°C for Animal 2). Furthermore, the stabilized level of 47.97°C falls within the heating window of 45°C to 50°C reported for the preclinical thermal treatments by Capistrano et al. (2020).

In contrast, the average temperature of the surrounding healthy tissue, shown in Figure 1 in the model, exhibits an extremely modest increase, stabilizing at 38.18°C at the end of the 1,800-second simulation. This behavior of healthy tissue, maintained comfortably below the critical threshold for thermal damage of 43°C, is consistent with the safety readings reported by Rodrigues (2017) in regions distant from the tumor, such as the animal's rectum and abdomen, which ranged up to 37.5°C. This marginal attenuation is due to the active cooling role played by healthy blood perfusion, which benefits from the slight increase in temperature. The formation of a steep and well-defined thermal gradient between the tumor and the healthy margins demonstrates the high spatial selectivity of energy deposition by the nanoparticles.

Furthermore, analysis of the microvascular response to thermal stress reveals highly contrasting and selective nonlinear behavior between regions. As illustrated in the time-course graphs of the tumor and healthy tissue in Figure 2, blood perfusion responds asymmetrically to heating.

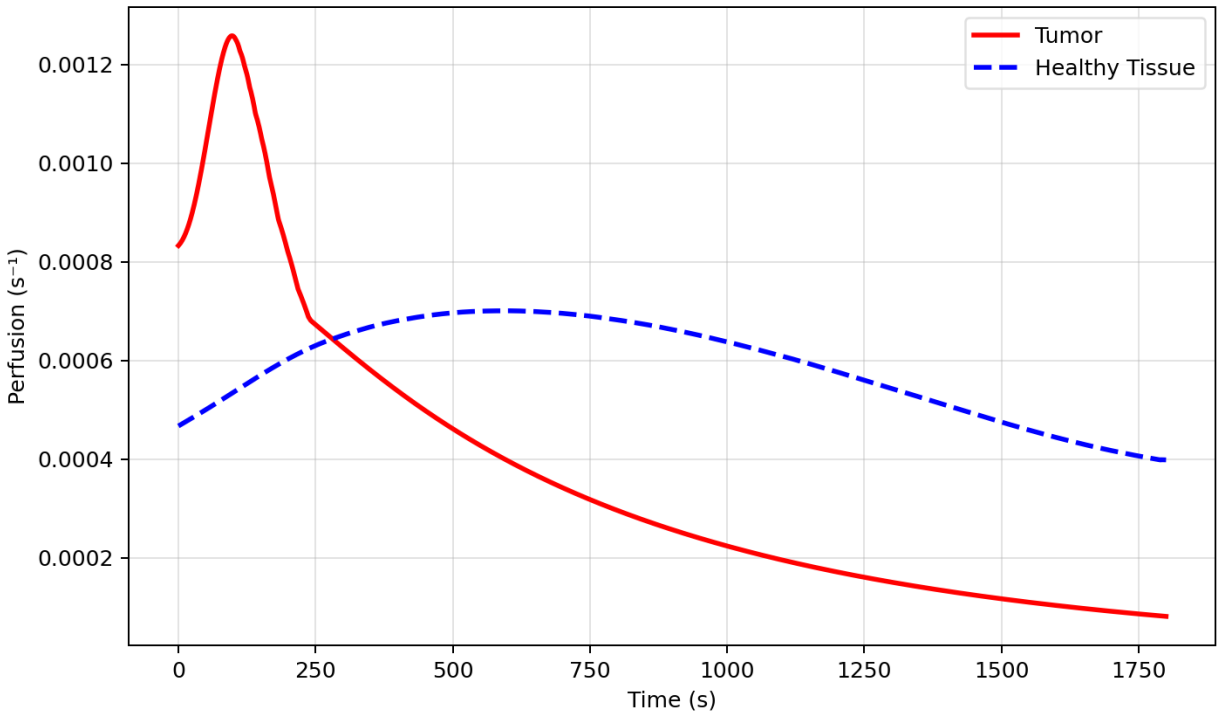


Figure 2: Graphic showing the temporal changes in blood perfusion in the different regions.

In the tumor, starting from a baseline rate of 8.33×10^{-4} s^{-1}, a gradual increase is observed in the initial moments due to an early heat-induced vasodilation response, reaching a peak of 1.28×10^{-3} s^{-1} at 98 seconds into the simulation. Immediately afterward, as thermal damage accumulates, tumor perfusion begins a sharp and progressive decline, culminating in a drop of approximately 90.31% at the end of treatment. This severe collapse is desirable because, by interrupting local blood flow, it eliminates the primary cooling mechanism, trapping the heat generated by the nanoparticles within the tumor core and optimizing the selectivity and efficiency of ablation.

In contrast, in the surrounding healthy tissue, the initial perfusion rate of 4.67×10^{-4}s^{-1} shows a continuous and much more prolonged increase as heating subsides, reaching a peak of 7.01×10^{-4}s^{-1} around 600 seconds — an increase of 49.89%. Although it undergoes a late decrease of approximately 14.35% due to prolonged thermal exposure, the final perfusion in healthy tissue remains at a level significantly higher than that of the tumor, preserving thermoregulatory capacity and protecting adjacent tissues from irreversible collateral damage.

These vascular dynamics are consistent with the relevant literature. Although Rodrigues (2017) simplified blood perfusion as zero in his one-dimensional analytical model to enable closed-form mathematical solutions, his review of preclinical trials reports that heating solid tumors in rodents above 43°C causes severe microvascular damage and ablative stasis, whereas neighboring normal tissues are capable of increasing their perfusion by factors of 1.8 to 5 times, respectively, to dissipate excess heat.

Additionally, early vascular collapse aligns with the numerical model by Capistrano et al. (2020), based on the Erdmann equations coupled with Arrhenius damage. In their study, the authors demonstrated that subcutaneous solid tumors are best described by low-perfusion regimes with accelerated microvascular collapse. Therefore, the successful computational reproduction of these opposing vascular responses confirms the simulator's physiological accuracy.

Furthermore, as shown in Figure 3, the model indicates that the first points located in the tumor core exceed the critical threshold for irreversible tissue damage ($\theta \geq 0.75$) exactly 449 seconds into treatment. From that point on, cell death accelerates in a typically sigmoid pattern due to the exponential dependence on temperature. At the end of the 1,800-second simulation, 100% of the tumor points exceed the threshold for irreversible necrosis, achieving complete ablation of the tumor mass starting at 1,780 seconds. The average degree of tissue damage in the tumor reaches a maximum value of 0.988, confirming the near-complete destruction of the tissue.

In contrast, the surrounding healthy tissue remained fully protected, showing no irreversible damage. No point exceeded the safety threshold of In contrast, the surrounding healthy tissue remained fully protected, showing no irreversible damage. No point exceeded the safety threshold of $\theta \geq 0,75$ at any time during therapy. The mean Arrhenius parameter in the healthy region reached a maximum value of 0.336, falling within the range of sublethal and reversible damage.

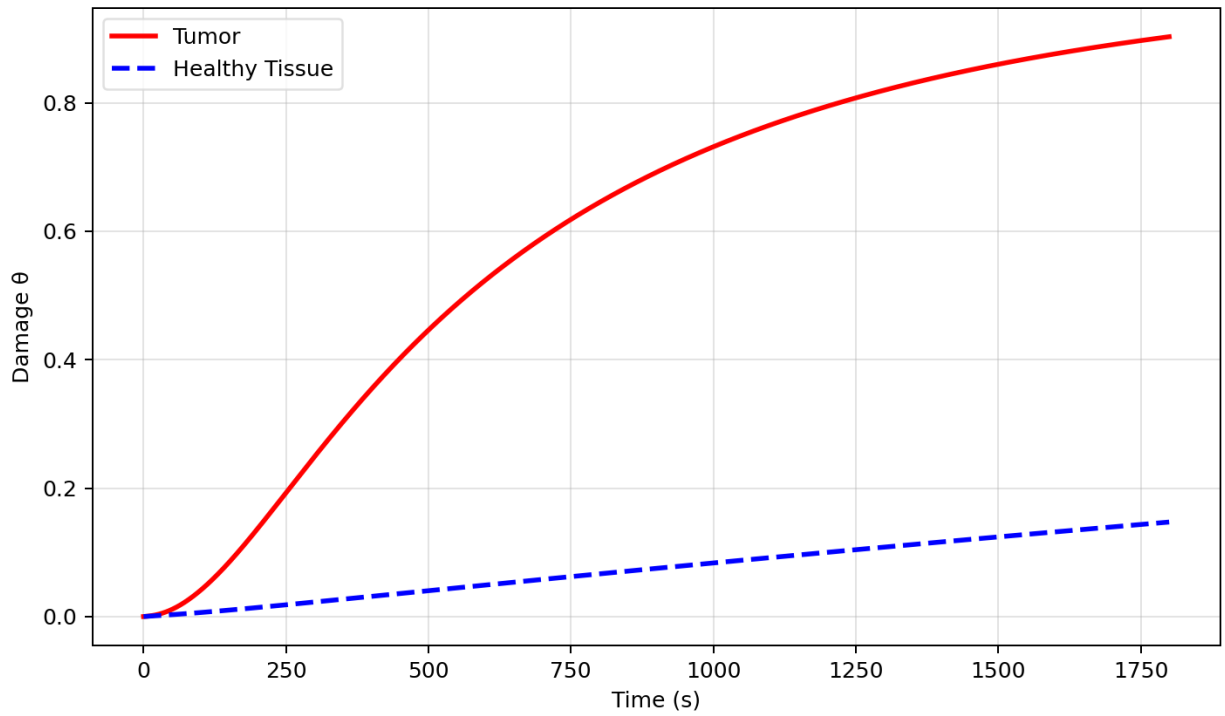


Figure 3: Graphic showing the change in damage over time in different regions.

When comparing our results with those of Capistrano et al. (2020), we observed that, upon evaluating the history of the animals subjected to 30 minutes of treatment, the authors demonstrated a direct correlation between the simulated damage fraction and the clinical outcome, showing that the mice that achieved complete tumor remission were those whose simulated necrosis volumes reached fractions of 100% and 96.2%, respectively. Thus, the numerical result obtained in the simulation—100% of the tumor volume with damage ≥ 0.75 and an average damage of 0.988—places the outcome of the proposed computational protocol at a level of efficacy equivalent to the cure and complete remission profile observed in the animals from the study by Capistrano et al. (2020). Additionally, the safety margin for healthy tissue is ensured by maintaining the average healthy damage at strictly reversible levels, with collateral tissue loss restricted to only 4.9% of points at the narrow peritumoral interface, which were controlled-sacrificed to guarantee the total elimination of the neoplastic margin.

Furthermore, the spatial distribution of temperature, shown in the map in Figure 4, reveals a radial structure with a very hot central core—corresponding to the tumor—and a decreasing thermal gradient toward the periphery. The tumor region appears as a well-defined hotspot, with temperatures exceeding 45°C. Surrounding this core is a narrow transition zone, in which the temperature drops rapidly from approximately 49°C to values between 37°C and 39°C. This steep gradient is desirable, as it confines damage to the tumor bed and minimizes heating of healthy tissue. At the outermost edges of the map, no secondary hotspots are formed, which confirms the functional preservation of perfusion in normal tissue and the absence of unwanted heat accumulation.

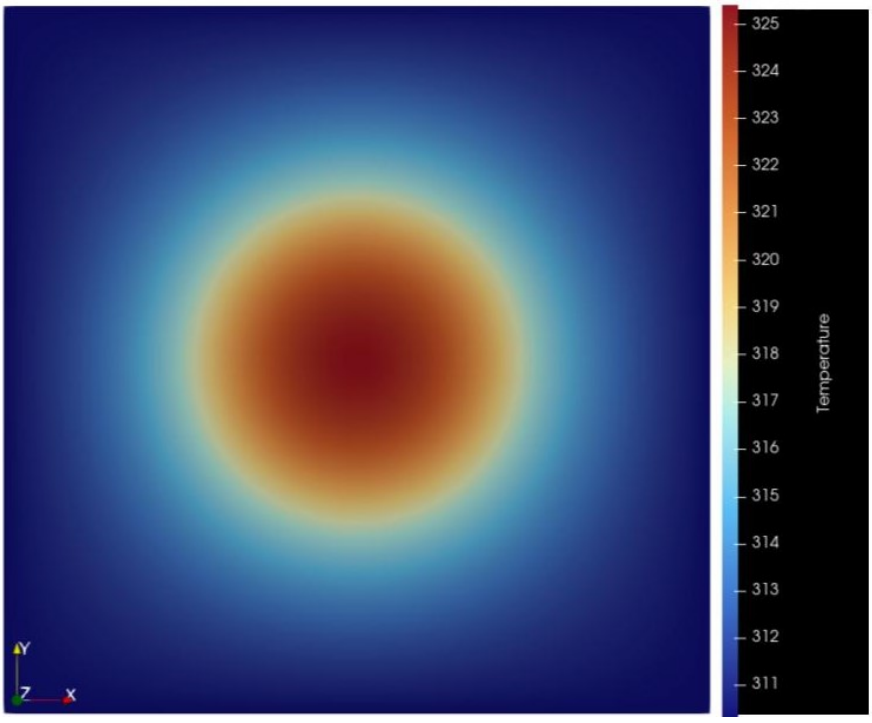


Figure 4: Cross-section of the temperature distribution map

In addition, the spatial analysis of the thermal dose expressed in CEM43 indicates that 83.33% of the total tumor volume accumulated a thermal dose greater than 240 minutes, accompanied by preservation of the surrounding healthy tissue, which did not reach a lethal CEM43 dose, reinforcing the notion that maintaining baseline levels of blood perfusion in healthy tissue protects these structures from heat. More specifically, the tumor reached an average dose of 1,503.75 minutes, with a maximum value of 9,506.38 minutes and a minimum of 160.71 minutes. In contrast, the surrounding healthy tissue recorded an average dose of 1.69 minutes (ranging from a minimum of 0.007 minutes to a maximum of 90.97 minutes near the tumor interface).

Conclusion

The establishment of magnetic hyperthermia as a clinically viable therapeutic modality faces challenges related to the lack of standardization and reproducibility of its protocols and to local thermal control, stemming from the extreme sensitivity of the physical heating phenomenon (Almeida; Campos; Castro, 2026). Minor experimental variations, such as fluctuations in the particle core diameter or deviations in magnetic field intensity, can unexpectedly alter the rate of heat dissipation.

Given this high parametric sensitivity, predictive numerical models serve as an important dosimetric resource for advancing the therapy, allowing for the analysis of complex transient dynamics and the determination of heating trends in a noninvasive manner. The use of a computational platform enables the exploration of a wide range of biological boundary conditions and physical parameters that would be difficult to achieve through purely experimental means. This model allows for the simulation of dozens of distinct scenarios through the systematic variation of its parameters.

As noted by Mak, Evaniew, and Ghert (2014), the success rate in translating rodent studies to clinical trials in cancer is less than 8%, due to profound differences between species. Thus, although the present simulation employs a simplified geometry, it faithfully reproduced the actual thermal dynamics observed in vivo, demonstrating that numerical simulations that are increasingly faithful to the microarchitecture of real tissue can represent a significant advance over studies using mice, overcoming the barriers identified by the authors. Consequently, it becomes possible to design and refine personalized therapeutic protocols rapidly and at low operational cost, which mitigates reliance on in vivo preclinical trials, reduces the need for animal sacrifice in the laboratory, and accelerates the safe transition of the technology to clinical trials.

Additionally, it was possible to observe the central role of the irregular blood perfusion in neoplastic tissue. Due to the irregular architecture of the tumor vasculature compared to healthy tissue—which poses a challenge for chemotherapy and radiation therapy—the efficiency of the primary mechanism for heat dissipation and temperature reduction in the region was extremely low, such that severe damage to the vasculature accumulated within minutes, leading to its inevitable collapse. In contrast, the opposite process is observed in the adjacent healthy tissue: perfusion benefits from the rise in temperature and becomes even more efficient at protecting the tissue.

References

Almeida MFM, Campos SS, Castro LM. Hipertermia magnética como terapia oncológica de precisão: uma revisão crítica. Rev Binacional Brasil-Argentina. 2026; https://doi.org/10.22481/rbba.v16i1.18632

Capistrano G, Rodrigues HF, Zufelato N, Gonçalves C, Cardoso CG, Silveira-Lacerda EP, et al. Noninvasive intratumoral thermal dose determination during in vivo magnetic nanoparticle hyperthermia: combining surface temperature measurements and computer simulations. Int J Hyperthermia. 2020;37(3):120–140. https://doi.org/10.1080/02656736.2020.1826583

Grauer O, Jaber M, Hess K, Weckesser M, Schwindt W, Maring S, et al. Combined intracavitary thermotherapy with iron oxide nanoparticles and radiotherapy as local treatment modality in recurrent glioblastoma patients. J Neurooncol. 2019;141(1):83–94. https://doi.org/10.1007/s11060-018-03005-x

Johannsen M, Gneveckow U, Thiesen B, Taymoorian K, Cho CH, Waldöfner N, et al. Thermotherapy of prostate cancer using magnetic nanoparticles: feasibility, imaging, and three-dimensional temperature distribution. Eur Urol. 2007;52(6):1653–1662. https://doi.org/10.1016/j.eururo.2006.11.023

Kainz W, Neufeld E, Bolch WE, Graff CG, Kim CH, Kuster N, et al. Advances in computational human phantoms and their applications in biomedical engineering: a topical review. IEEE Trans Radiat Plasma Med Sci. 2019;3(1):1–23. https://doi.org/10.1109/TRPMS.2018.2883437

Maier-Hauff K, Ulrich F, Nestler D, Niehoff H, Wust P, Thiesen B, et al. Efficacy and safety of intratumoral thermotherapy using magnetic iron-oxide nanoparticles combined with external beam radiotherapy on patients with recurrent glioblastoma multiforme. J Neurooncol. 2011;103(2):317–324. https://doi.org/10.1007/s11060-010-0389-0

Mak IWY, Evaniew N, Ghert M. Lost in translation: animal models and clinical trials in cancer treatment. Am J Transl Res. 2014;6(2):114–118.

Maniotis N, Maragakis M, Vordos N. A comprehensive analysis of nanomagnetism models for the evaluation of particle energy in magnetic hyperthermia. Nanoscale Adv. 2025;7(14):4252–4269. https://doi.org/10.1039/d5na00258c

Matsumi Y, Kagawa T, Yano S, Tazawa H, Shigeyasu K, Takeda S, et al. Hyperthermia generated by magnetic nanoparticles for effective treatment of disseminated peritoneal cancer in an orthotopic nude-mouse model. Cell Cycle. 2021;20(12):1122–1133. https://doi.org/10.1080/15384101.2021.1919441

Peeken JC, Vaupel P, Combs SE. Integrating hyperthermia into modern radiation oncology: what evidence is necessary? Front Oncol. 2017;7:132. https://doi.org/10.3389/fonc.2017.00132

Pennes HH. Analysis of tissue and arterial blood temperatures in the resting human forearm. J Appl Physiol. 1948;1(2):93–122. https://doi.org/10.1152/jappl.1948.1.2.93

Rego GNA, Mamani JB, Souza TKF, Nucci MP, Silva HR, Gamarra LF. Therapeutic evaluation of magnetic hyperthermia using Fe3O4-aminosilane-coated iron oxide nanoparticles in glioblastoma animal model. Einstein (Sao Paulo). 2019;17(4):eAO4786. https://doi.org/10.31744/einstein_journal/2019AO4786

Rodrigues HF, Capistrano G, Bakuzis AF. In vivo magnetic nanoparticle hyperthermia: a review on preclinical studies, low-field nano-heaters, noninvasive thermometry and computer simulations for treatment planning. Int J Hyperthermia. 2020;37(3):76–99. https://doi.org/10.1080/02656736.2020.1800831

Rosensweig RE. Heating magnetic fluid with alternating magnetic field. J Magn Magn Mater. 2002;252:370–374. https://doi.org/10.1016/S0304-8853(02)00706-0

Santos MO, Lima FCS, Martins LFL, Oliveira JFP, Almeida LM, Cancela MC. Estimativa de incidência de câncer no Brasil, 2023-2025. Rev Bras Cancerol. 2023;69(1):e-213700. https://doi.org/10.32635/2176-9745.RBC.2023v69n1.3700

Sapareto SA, Dewey WC. Thermal dose determination in cancer therapy. Int J Radiat Oncol Biol Phys. 1984;10(6):787–800. https://doi.org/10.1016/0360-3016(84)90379-1

Singh M, Singh T, Soni S. Pre-operative assessment of ablation margins for variable blood perfusion metrics in a magnetic resonance imaging based complex breast tumour anatomy: simulation paradigms in thermal therapies. Comput Methods Programs Biomed. 2021;198:105781. https://doi.org/10.1016/j.cmpb.2020.105781

Vicentini M, Vassallo M, Ferrero R, Androulakis I, Manzin A. In silico evaluation of adverse eddy current effects in preclinical tests of magnetic hyperthermia. Comput Methods Programs Biomed. 2022;223:106975. https://doi.org/10.1016/j.cmpb.2022.106975

Vilas-Boas V, Carvalho F, Espiña B. Magnetic hyperthermia for cancer treatment: main parameters affecting the outcome of in vitro and in vivo studies. Molecules. 2020;25(12):2874. https://doi.org/10.3390/molecules25122874